Received 18 July 2023; revised 21 August 2023; accepted 25 August 2023. Date of publication 28 August 2023; date of current version 3 October 2023.

Digital Object Identifier 10.1109/OJAP.2023.3309375

Multi-Mode Antennas for Ultra-Wide-Angle Scanning Millimeter-Wave Arrays

GABRIELE FEDERICO [1] (Graduate Student Member, IEEE), ZHE SONG [2] (Senior Member, IEEE), GUILHERME THEIS [1] (Graduate Student Member, IEEE), DIEGO CARATELLI [1,3] (Senior Member, IEEE), AND A. BART SMOLDERS [1] (Senior Member, IEEE)

[1]Department of Electrical Engineering, Eindhoven University of Technology, 5600 MB Eindhoven, The Netherlands

[2]RFFE Department, Qualcomm Technologies, 6546 AS Nijmegen, The Netherlands

[3]Department of Research and Development, The Antenna Company, 5656 AE Eindhoven, The Netherlands

CORRESPONDING AUTHOR: G. FEDERICO (e-mail: g.federico@tue.nl)

This work was supported by the framework of the Top Consortium Knowledge and Innovation (TKI) Project Arrays 5G running jointly at The Antenna Company and Eindhoven University of Technology.

ABSTRACT In this paper, a novel multi-mode millimeter-wave antenna array with enhanced scan range and reduced scan losses is presented. The individual array element consists of a differentially fed microstrip patch on top of which a cylindrical dielectric resonator is integrated. The radiation pattern of the antenna element can be reconfigured by changing the phase offset between the feeding ports of the patch and the dielectric resonator to excite two distinct radiating modes. With such a feature, the field of view can be divided into two different subspaces, with the first one covering the angular range from $-75°$ to $0°$ and the second one from $0°$ to $+75°$. In a 1×16 linear array configuration, the achieved scan range extends from $-75°$ to $75°$ along the horizontal plane with a maximal gain loss of 3 dB, which is better than the ideal $\cos\theta_0$ behavior. The proposed design operates in the frequency range between 27 GHz and 29.5 GHz and, thanks to its wide-scan capabilities, constitutes an effective solution for upcoming 5G/6G millimeter-wave wireless communications.

INDEX TERMS mm-wave communications, multi-mode antenna, phased antenna array, reconfigurable antenna, wide-angle scanning.

I. INTRODUCTION

PHASED array antennas constitute key components of millimeter-wave (mm-wave) wireless systems thanks to their electronic beam-steering capabilities. They are employed in a variety of applications such as satellite communications, radar, space exploration, and remote sensing, as well as in emerging 5G/6G technologies which can benefit from high antenna gain to compensate for the larger propagation losses experienced at mm-wave frequencies.

The design of phased arrays poses a number of challenges that need to be addressed. One of the most significant drawbacks which this class of radiating structures is typically subject to is the limited scan range. According to theory, the scan capabilities of an array are limited by the beamwidth of the embedded element pattern. In the ideal case, the array gain decays following a $\cos\theta_0$ trend, where θ_0 denotes the scan angle. The most common solutions adopted in the design of wide-angle scanning arrays are microstrip patch antennas which typically feature a beamwidth of $110°$ and can therefore enable a scan range of $\pm 55°$ both in azimuth and elevation with a typical maximum gain loss of 4-5 dB when integrated into an array configuration [1].

Furthermore, when scanning toward the end-fire region, the increase of mutual coupling between array elements causes a fast degradation of efficiency and gain antenna characteristics. Many studies were carried out to reduce the

mutual coupling between elements, for example, by introducing a metal cavity [2] between the adjacent antenna elements or metal vias [4] as a separating structure. In [3], instead, wide-angle scanning performance is achieved by using high-impedance periodic structures that suppress surface waves while broadening the embedded element radiation pattern.

Another approach to improve the scan performance of antenna arrays relies on the enhancement of the beamwidth of the embedded element pattern. Different design concepts are available in the scientific literature [5], [6], [7], [8], [9]. In [5], two metal walls are introduced on the side of the basic patch antenna element to increase the relevant beamwidth up to 120°. In [6], a large beamwidth is achieved with a U-shaped microstrip antenna enclosed with two metal walls integrated in the plane opposite to the scan direction of the linear array.

Another approach to achieve wide scanning is to use pattern-reconfigurable antennas. The working principle is based on the segmentation of the scan range in sub-spaces, where each sub-space is covered by steering the embedded element pattern based on different modal configurations. Usually, pattern reconfiguration is realized by introducing pin diodes to switch between radiating modes [7]. This approach removes the need for broadening the beamwidth of the embedded element pattern and can benefit from more directive radiating modes, thus enabling an additional advantage in filtering out undesired grating lobes.

Different from the reconfigurable antenna technology, metamaterial-based lens design methodologies can result in broader scan ranges as compared to traditional arrays thanks to the integration of metamaterial structures [8], [9]. As a matter of fact, metamaterials can enable unconventional electromagnetic wave propagation properties by controlling permittivity and permeability independently in a complex way [10]. However, metamaterial lenses are typically very complex and large, which is undesired for onboard applications.

When considering the mm-wave frequency range, most of the listed methods above are not easy to realize because of manufacturing limitations or extra losses introduced by passive components.

In this paper, we propose a wide-scanning array topology based on a novel two-port multi-mode antenna element realized by integrating a pin-fed dielectric resonator (DR) with a capacitively fed microstrip patch. In our design, the mode switching is realized by selecting different phase offsets at the antenna feeding ports. The proposed antenna solution has been implemented in a linear array that can switch between two radiating modes: the first mode covering the sub-space from $-75°$ to $+20°$ when the two ports of the individual array element are fed with the same phase and the second mode covering the sub-space from $-20°$ to $+75°$ when the ports are fed with an offset of 180°. In the presented design, no switches are required to modify the current paths along the antenna structure; to this end, use is made of multi-channel beamforming RF integrated circuits (RFICs) with integrated vector modulators, which are readily available on the market nowadays [11]. In this way, a 1×16 linear array of the developed antenna can scan in the angular range from $-75°$ to $+75°$ with a maximal scan loss of only 3 dB.

This paper is organized as follows: Section II concerns the antenna element design and discusses the working principle with the related theory and the geometry of the radiating structure. Section III details the simulation and measurement results of the 1×16 linear array. In Section IV, the proposed solutions is benchmarked against the state of the art, and Section V concludes with some final remarks.

II. PRINCIPLE AND ANALYSIS OF THE ANTENNA ELEMENT

For point-to-multipoint wireless communications, phased arrays with wide-angle scanning capabilities are usually preferred. The scanning capability of an antenna array is mostly determined by the embedded element pattern. Consider a linear array of N elements. The array pattern $\vec{S}(\theta_0)$ can be expressed as a multiplication of the ideal array factor and the element factor $\vec{f}(\theta_0)$:

$$\vec{S}(\theta_0) = \vec{f}(\theta_0) \sum_{n=1}^{N} e^{-j[(n-1)k_0 d \sin(\theta_0) - \psi_n]} \tag{1}$$

upon adopting a suitable spherical coordinate reference system and assuming a θ_0-only dependence. In (1), d is the distance between the elements, k_0 is the wave number in free space, and ψ_n denotes the phase offset applied to each array port. As the beam is steered towards larger angles, the array gain is attenuated proportionally to the element pattern. For this reason, antenna elements with a wide half-power beamwidth (HPBW) are often employed to realize wide-angle scanning arrays [1].

In order to extend the scan range above the physical limit of $\cos\theta_0$, in this work, we will investigate the use of antenna elements with two radiating modes. By multi-mode antenna, we mean a single physical radiator with separate feeding ports that excite different characteristic modes. In this way, the field of view can be divided into two sub-spaces, where each sub-space is covered by one of two radiating modes.

The radiation pattern scanning capabilities of an array based on a multi-mode antenna concept are illustrated in Fig. 1 in the particular case of two radiating modes, both characterized by a $\cos^2(\theta_0)$ element pattern behavior as an example. Each radiating mode identifies a different sub-space where the array beam is scanned. As one can notice, the overall scan range is broadened as compared to a traditional array implementation while attenuating the impact of unwanted grating lobes. Such a feature of multi-mode antennas allows for the integration in an array configuration without the need to keep an inter-element spacing of $\lambda_0/2$ or smaller, with λ_0 being the wavelength in free space. This enables additional degrees of freedom in the design process that can be favorably exploited to enhance array performance in terms of scan loss mitigation.

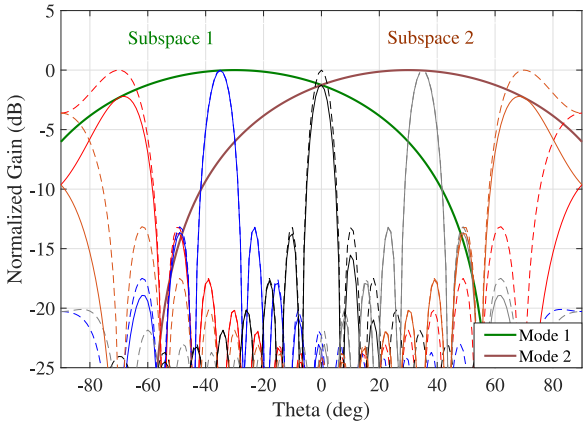

FIGURE 1. Array scanning when two radiating modes are used in the array pattern multiplication formula with the array factor (in dashed line).

A. THEORY

To realize a multi-mode antenna based on a phase control principle, we make use of the combination of an electric and a magnetic dipole with orthogonal orientation.

The total far-field of a pair of orthogonal electric and magnetic dipoles can be obtained by superimposing their individual far-fields because these are orthogonal to each other [12], [13]. Therefore, the total E_θ and E_ϕ components of a z-directed electric dipole (length l_e, current amplitude I_e) and a y-directed magnetic dipole (length l_m, current amplitude I_m) are given by [12]:

$$E_{T_\theta} = \frac{k}{4\pi r} e^{-jkr}\left(j\eta I_e l_e \sin\theta - e^{j\delta} j I_m l_m \cos\phi\right) \quad (2)$$

$$E_{T_\phi} = \frac{k}{4\pi r} e^{-jkr} e^{j\delta} j I_m l_m \cos\theta \sin\phi \quad (3)$$

where we assume time-harmonic fields and where $k = \omega\sqrt{\epsilon_0\mu_0}$ is the wave number, and δ is the phase offset between the two ports of the same element. Upon assuming $\eta l_e I_e = l_m I_m = lI$, the expression of the total electric field, given by:

$$|E_T| = \sqrt{|E_{T_\theta}|^2 + |E_{T_\phi}|^2}, \quad (4)$$

can be simplified as:

$$|E_T| \propto \sqrt{\sin^2\theta + \cos^2\phi - 2\sin\theta\cos\phi + \cos^2\theta\sin^2\phi} \quad (5)$$

when $\delta = 180°$, and:

$$|E_T| \propto \sqrt{\sin^2\theta + \cos^2\phi + 2\sin\theta\cos\phi + \cos^2\theta\sin^2\phi} \quad (6)$$

when $\delta = 0°$.

According to the equations above, the maximum and minimum of $|E_T|$ are located along the $\pm x$-direction. One can notice that E_T reaches its maximum intensity along $\theta = 90°$ for $\delta = 0°$, and along $\theta = -90°$ for $\delta = 180°$ as pointed out in [12], where the objective was to synthesize an end-fire-like radiation pattern.

The simplified basic principle is illustrated in Figs. 2a and 2b, where the effect of the superposition of an electric dipole along the z-axis and a magnetic dipole along the y-axis is shown in case of the same feeding phase and in case of a phase offset of 180°, respectively. However, it is worth mentioning here that the simplified illustration above makes use of ideal electric and magnetic dipoles but, in reality, the actual radiation patterns will be different, depending on the specific antenna design implementation. For example, when we integrate such an antenna in an array configuration, the direction of maximum radiation will be slightly steered towards the direction of $\theta = 45°$ due to the presence of the ground plane and the adjacent elements. It is important to mention that the design proposed in [12] cannot support two independent radiating modes and, therefore, cannot be used to enhance the scan range of an antenna array using the system architecture and principle described in this research study. To achieve such a goal, one should use a suitable multi-port antenna solution, such as the one detailed in the following sub-sections.

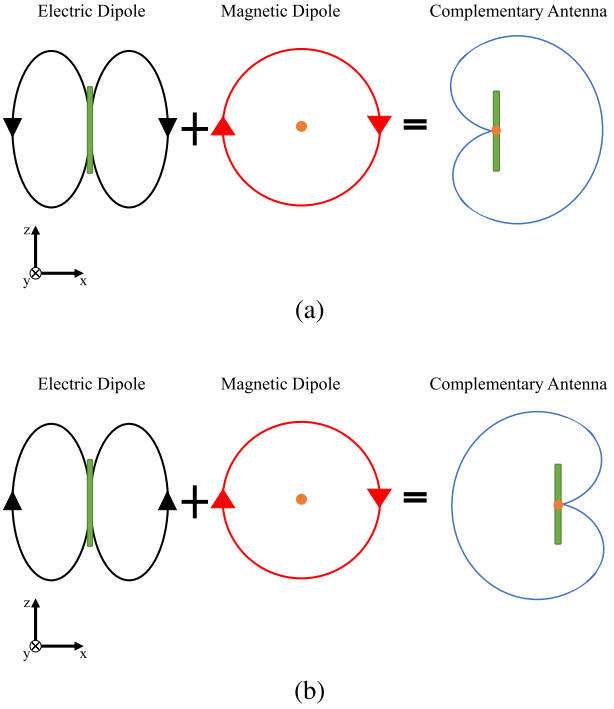

FIGURE 2. Basic principle of two complementary unilateral antennas with *E*-Field of a *z*-directed electric dipole and with *H*-Field of a *y*-directed magnetic dipole (a) in case of same feeding phase between the two ports and (b) in case of 180° phase offset between the two ports.

B. MULTI-MODE ANTENNA GEOMETRY

The novel multi-mode antenna element that we propose in this study consists of a differentially fed loaded microstrip patch integrated with a pin-fed cylindrical DR. Such an antenna can support multiple radiating modes by selecting different phase offsets between the two ports. The antenna structure is sketched in Fig. 3a and Fig. 3b, where the cylindrical DR is placed on top of the differentially fed patch element. In the aforementioned figures, the prepreg layers

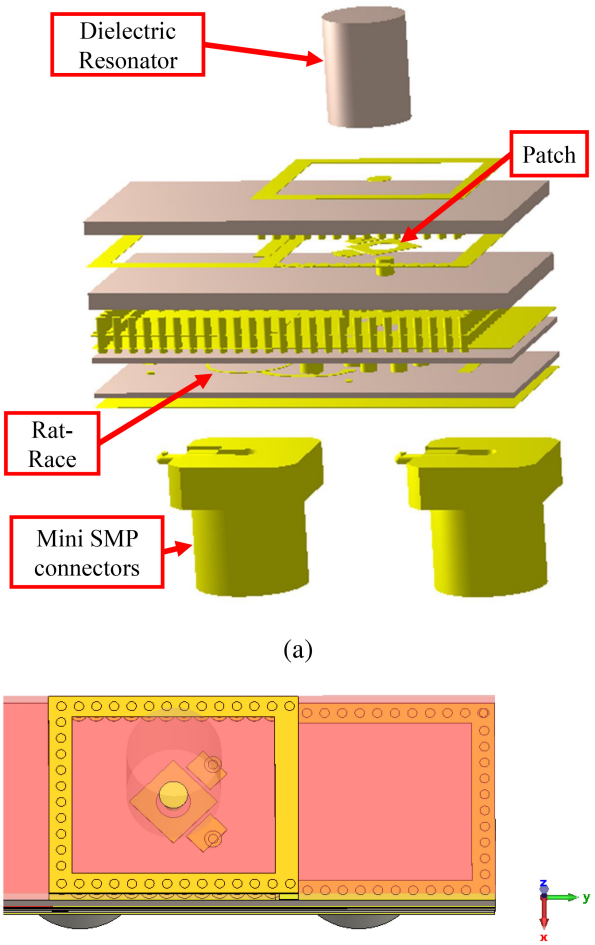

FIGURE 3. (a) Exploded view of the antenna structure with mini-SMP connectors and transparent prepeg layers and (b) Top view of the single element with transparent cylindrical DR.

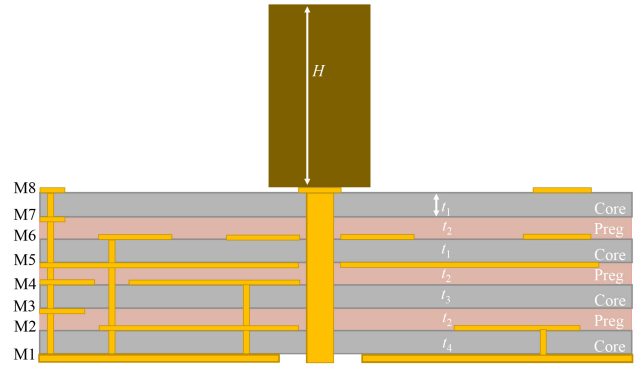

FIGURE 4. Single element stack-up.

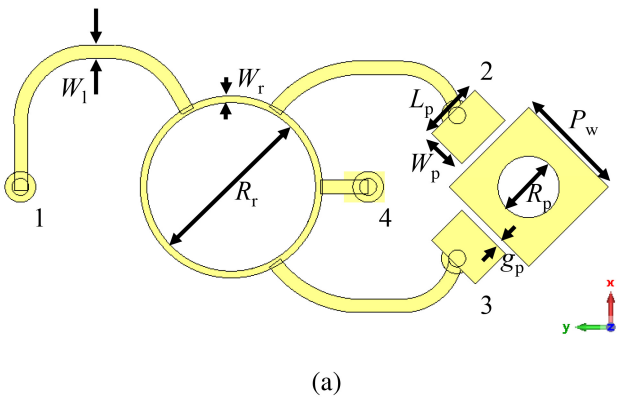

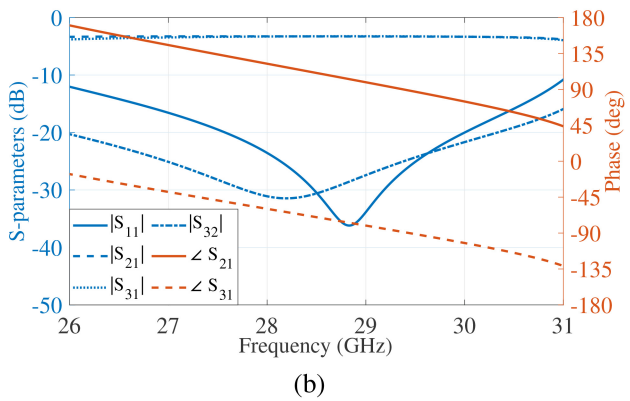

FIGURE 5. (a) Feeding network of the capacitively fed patch antenna realized with a rat-race power divider and (b) relevant scattering parameters.

are made transparent in such a way as to allow the view of the rectangular cavity that is realized by grounding the top and the bottom layers with through-via fences surrounding the entire structure. Such a cavity is useful to reduce the parasitic coupling level with nearby antenna elements when integrated in an array. The antenna ports are fitted with mini-SMP 18S142-40ML5 connectors to enable the passive characterization of the radiating structure.

The proposed antenna is built using 8 metal layers as shown in the printed circuit board (PCB) stack-up of Fig. 4. As one can notice, the Rogers RO4350B cores with relative permittivity $\epsilon_r = 3.66$ and loss tangent $\tan\delta = 0.0037$ at 10 GHz are interleaved with Rogers RO4450F prepreg layers with a thickness of 0.1 mm. From the bottom to the top, the four PCB layers have different thicknesses, equal to 0.168 mm, 0.168 mm, 0.508 mm, and 0.422 mm, respectively. The dielectric rod is instead realized with Rogers RO4360G2 material having $\epsilon_r = 6.3$ and $\tan\delta = 0.0023$; its height is 3.2 mm while the relevant diameter is 2.5 mm.

The patch structure is differentially fed by two metal pads located on metal layer 6 (M6), which are connected to the mini-SMP connector through a via feed. The size of the patch is 1.65 mm × 1.65 mm; a hole with a diameter of 0.9 mm is realized at its center to allow for the feeding pin of the DR to be inserted through it. The capacitively coupled metal pads have dimensions of 0.9 mm × 0.63 mm and are located at a distance of 0.125 mm from the patch. To implement the 180° phase offset between the two pads, the via feeds are connected to a rat-race coupler, as shown in Fig. 5a, located on metal layer 2 (M2). The optimized diameter of

TABLE 1. Relevant dimensions of the antenna structure.

Parameter	Dimension (mm)	Parameter	Dimension (mm)
W_l	0.2	t_1	0.422
W_r	0.1	t_2	0.508
R_p	0.9	t_3	0.168
W_p	0.63	t_4	0.168
g_p	0.125	T_l	1.27
L_p	0.9	P_w	1.65
R_r	2.57	H	3.2

the ring forming the rat-race is 2.57 mm to enforce out-of-phase signals at the two feeding probes, whereas the width of the transmission line is 0.1 mm to ensure a 70 Ω characteristic impedance level. The width of the 50 Ω transmission lines directly connected to the feeding vias is 0.2 mm. The relevant dimensions of the antenna structure are summarized in Table 1.

The central transmission line, corresponding to the decoupling port of the rat-race coupler, is terminated through a via pin with a 50 Ω resistor soldered on the bottom layer of the board. The simulated RF performance of the developed power divider is shown in Fig. 5b. As it can be noticed, excellent impedance matching characteristics have been achieved in the frequency range from 26 GHz to 31 GHz, in combination with the desired phase offset of 180° between the two output ports.

The DR is fed by a vertical via pin having diameter of 0.55 mm, and going through the entire PCB as illustrated in Fig. 4, and is directly connected to the mini-SMP connector.

C. SIMULATION RESULTS

The design and optimization of the antenna element and the relevant linear array have been carried out using the commercial electromagnetic field solver CST Microwave Studio ©.

The simulated electric and magnetic field distributions excited by the embedded antenna element are shown in Figs. 6a and 6b, respectively. As it appears in Fig. 6, the H-field forms basically a loop when the DR pin is fed, whereas the E-field is directed along the z-direction. As a matter of fact, the resonant mode excited by the vertical feeding pin in the DR is the fundamental one, TM^z_{011}. Conversely, when the patch port is excited, the E-field forms a loop, while the H-field is directed along the y-direction. This distribution corresponds to the TE^y_{111} fundamental mode. The first mode is equivalent to an electric dipole, and the second one to a magnetic dipole. Because of the orthogonality between the two dipoles, the coupling between the two ports is very low, typically below the level of −35 dB, in the frequency range between 26 GHz and 30 GHz, as it can be noticed in Fig. 7.

From Fig. 7, it can also be seen that the antenna element shows very broadband properties, with an impedance-matching bandwidth of 6 GHz around the center frequency of 27 GHz.

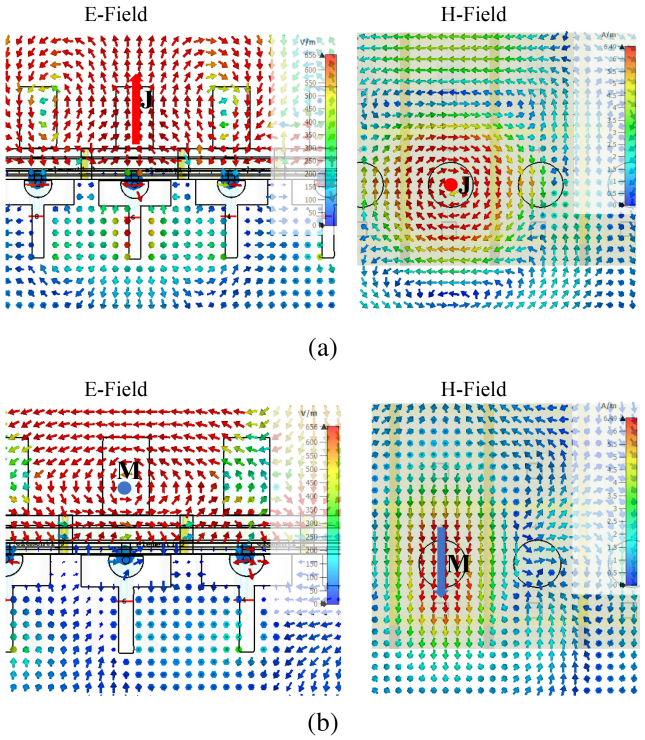

FIGURE 6. (a) E-Field and H-Field of the TM^z_{011} mode when the DR port of the embedded central element is activated and (b) E-Field and H-Field of the TE^y_{111} mode when the patch port of the embedded central element is activated.

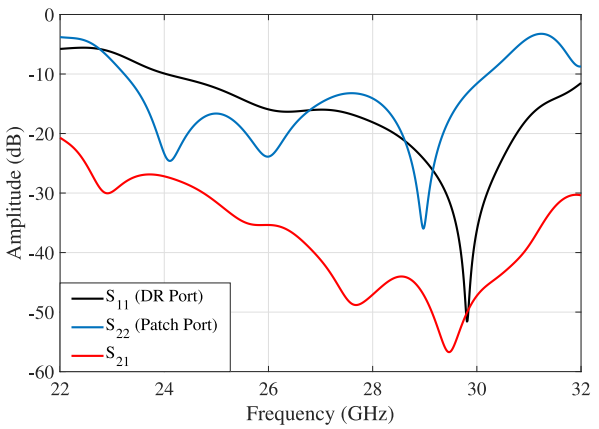

FIGURE 7. Simulated reflection coefficient of the single element and coupling between the two ports.

The simulated multi-mode characteristics of the proposed antenna element are illustrated in Fig. 8. In particular, we can notice how the element radiation pattern is steered towards the $-x$ direction when the relevant input ports are fed with the same phase and towards the $+x$ direction when a phase offset of 180° is enforced.

III. LINEAR ANTENNA ARRAY

The developed multi-mode antenna element has been integrated into a 1 × 16 linear array. The overall size of such an array is 80.55 mm × 13 mm × 4.88 mm, with the antenna

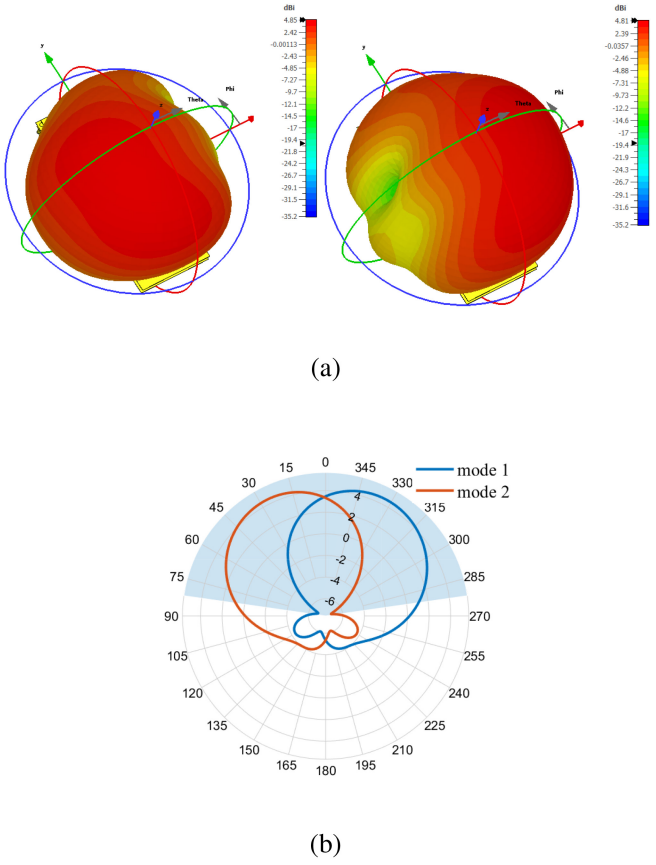

FIGURE 8. (a) 3D realized antenna gain of the two radiating modes of the single antenna element when both ports are fed with the same phase (on the left) and with a phase offset of 180° (on the right) and (b) 2D cut in the *xz*-plane.

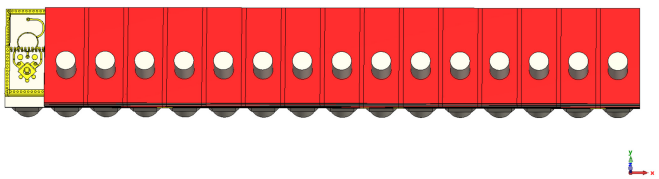

FIGURE 9. Simulation model of the 1 × 16 linear array.

elements being separated by a distance of 5 mm. The simulation model of the linear antenna array is shown in Fig. 9, where the upper layers of the first radiating element have been hidden in such a way as to allow the view of the relevant feeding network.

The simulated beam steering characteristics of the array are illustrated in Fig. 10, where the enlarged scan range from $-75°$ to $+75°$ along the elevation plane can be readily noticed. In order to highlight the radiation properties of the array in terms of scan losses, two dashed lines following the $\cos\theta_0$ and the $\cos^{0.5}\theta_0$ law, respectively, have been added. From basic theory, it is well known that conventional phased antenna arrays are subject to a gain degradation which follows a $\cos\theta_0$ law in the ideal case [1]. In the presented case, we want to highlight that the scan capabilities of the

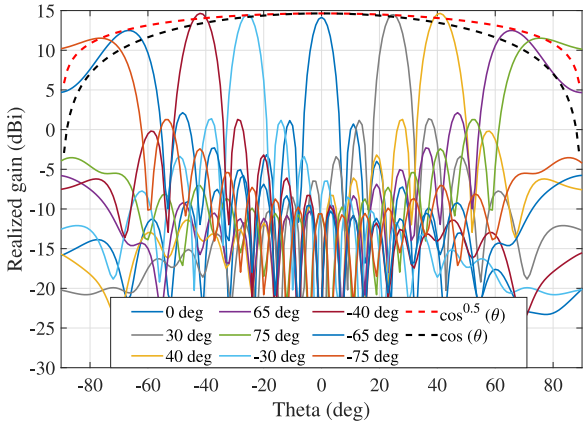

FIGURE 10. Simulated scan range of the linear array at 28 GHz.

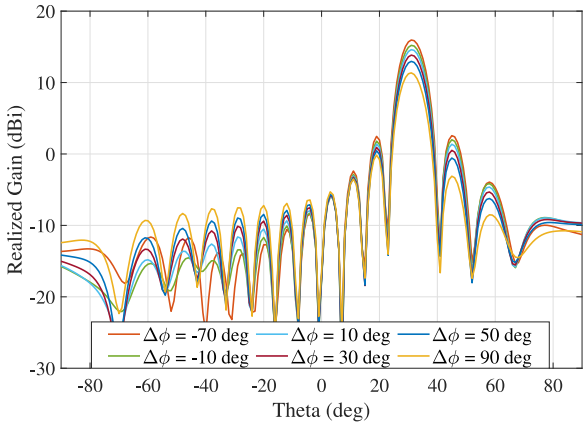

FIGURE 11. Improvement of SLL and peak gain by varying the phase difference between the two ports ($\Delta\phi$).

developed antenna array can outperform the ideal case without making use of complex and/or lossy solutions in the design, by only adjusting the phase offset between different antenna ports.

As mentioned above, in order to reach wide scanning capabilities, two radiating modes are excited by controlling the phase offset between the two feeding ports of the individual antenna array element. As it appears from Fig. 11, an optimal phase difference can be identified for each steering direction. Tailored phase offsets can lead not only to better performance in terms of realized gain but also in terms of side lobe level and, eventually, grating lobes.

In order to validate the simulation results, a physical prototype of the linear array has been realized. The manufactured demonstrator is shown in Fig. 12, where one can notice the white cylindrical DRs mounted on the top of the PCB and the mini-SMP connectors soldered on the bottom. The PCB is instead covered by a black solder mask.

The gain pattern measurement setup is shown in Fig. 13 where the antenna array is placed at the center of a mm-wave anechoic chamber which uses an open-ended waveguide as a probe [14]. A spherical scan in the far-field region of the device under test is performed so to measure the co- and

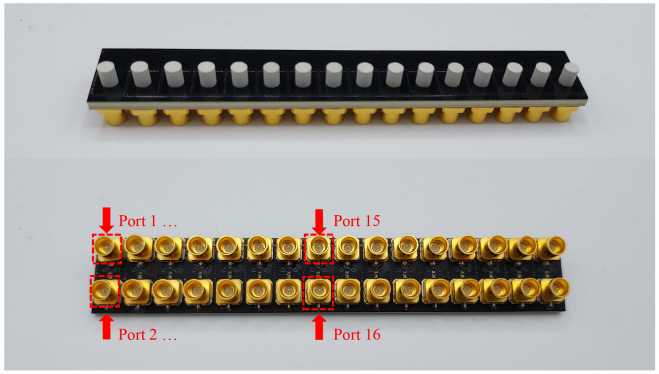

FIGURE 12. Top and bottom views of the manufactured linear array.

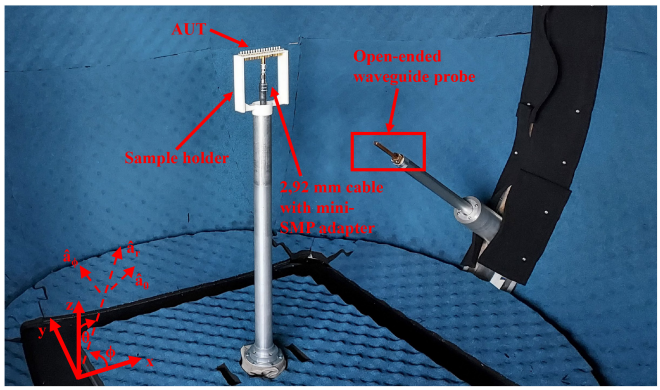

FIGURE 13. Antenna under test (AUT) at the center of the mm-wave anechoic chamber.

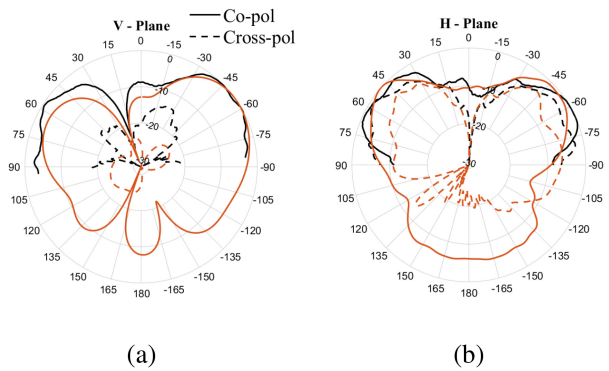

FIGURE 14. Measured (black) and simulated (orange) normalized gain pattern of the central element at 28 GHz, in the (a) $\phi = 90°$-plane and (b) in the $\phi = 0°$-plane when port 15 is fed and all the other ports terminated on 50 Ω loads.

cross-polarized components of the gain along both the *E*- and *H*-planes. To this end, a suitable mini-SMP adapter was used to characterize each antenna port, while the other ports were terminated with 50 Ω loads.

For the sake of conciseness, only the measured characteristics of the central array element at 28 GHz are plotted and compared to the simulated results. Fig. 14 shows the normalized gain pattern of the 8-th element embedded in the linear array along the *xz*-plane (see Fig. 14a) and the *yz*-plane (see Fig. 14b) when the DR port is fed, while Fig. 15 shows the

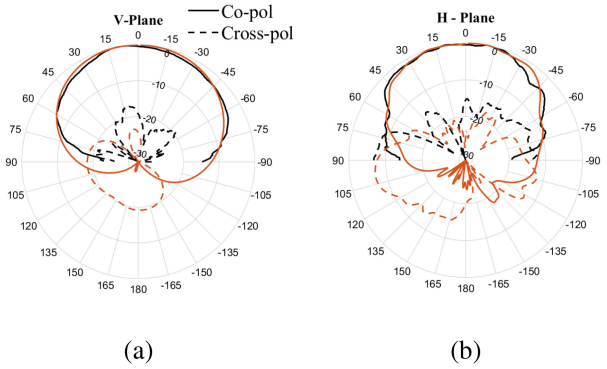

FIGURE 15. Measured (black) and simulated (orange) normalized gain pattern of the central element at 28 GHz, in the (a) $\phi = 90°$-plane and (b) in the $\phi = 0°$-plane when port 16 is fed and all the other ports terminated on 50 Ω loads.

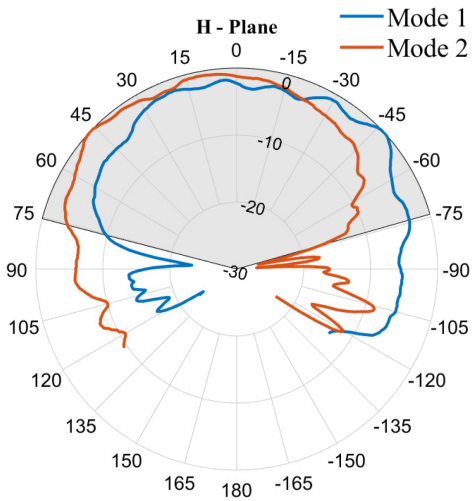

FIGURE 16. Illustration of the two radiating modes of the central element with the total 3 dB HPBW highlighted in gray.

normalized gain pattern when the patch port is fed. In both cases, simulation and measurement results are in excellent agreement.

To evaluate the total embedded radiation pattern of each individual array element, the two relevant patterns are combined by post-processing through the following equations:

$$\vec{f}_{\theta_T} = \left(f_{1_\theta} + f_{2_\theta}\right)\vec{a}_\theta \tag{7}$$

$$\vec{f}_{\phi_T} = \left(f_{1_\phi} + f_{2_\phi}\right)\vec{a}_\phi \tag{8}$$

$$|\vec{f}_T| = \sqrt{|\vec{f}_{\theta_T}|^2 + |\vec{f}_{\phi_T}|^2} \tag{9}$$

where f_{1_θ} and f_{2_θ} are the θ-components of the element pattern when the DR-port and the patch-port are fed, respectively; in the same way, f_{1_ϕ} and f_{2_ϕ} are the ϕ-components of the radiation pattern when the DR-port and the patch-port are fed, respectively. Furthermore, $\vec{a}_\theta$ and $\vec{a}_\phi$ are the unit vectors in the θ and ϕ direction, respectively.

The combined radiation pattern coverage is shown in Fig. 16. By controlling the phase offset at the input ports, it is possible to excite a different radiating mode and, in this way, illuminate a different angular region. In particular,

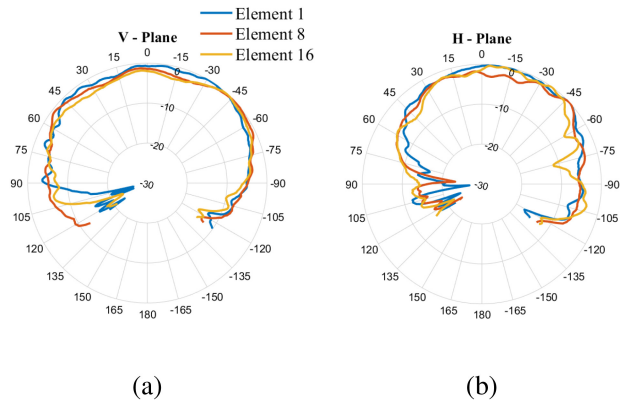

FIGURE 17. Normalized gain pattern of the two corner elements and the central element at 28 GHz, (a) in the V-plane and (b) in the H-plane with the two ports fed without phase offset.

mode 1 is characterized by an HPBW ranging from −75° to +20°, while Mode 2 has an HPBW ranging from +75° to −20°.

By combining the two radiating modes, one can achieve an overall HPBW of 150° that is useful to enable wide-angle scanning at the array level.

Fig. 17 shows the combined radiation patterns of the two corner elements and the central element along the *yz*-plane (17a) and *xz*-plane (17b), respectively. The gain pattern of element 1 shows a larger ripple level which is caused by the proximity to the truncation of the ground plane at the corner of the PCB structure.

The measured reflection coefficients of the central element are shown in Fig. 18. In order to perform the S-matrix measurement, suitable adapters, and cable jumpers were adopted. The scattering parameters have been evaluated upon de-embedding the effect of the aforementioned transitions connected between the Vector Network Analyser (VNA) cable and the antenna ports using the method described in [23]. This is illustrated in Fig. 18, where the simulated reflection coefficient is compared to the measured one using the cable and the adapter only.

The measurement results in both cases follow the trend of the simulation results, with the only exception of a shift of the resonance around 29 GHz towards higher frequencies (see Fig. 18). This effect results in a reflection coefficient with a magnitude above −10 dB in the frequency range between 26.5 GHz and 28.5 GHz (see Fig. 18b). This is caused by manufacturing tolerances as it has been verified by numerical simulations.

With the same measurement setup and by using the same de-embedding methodology, the isolation between the central antenna element and the adjacent ones has been characterized. The results are plotted in Fig. 19a and Fig. 19b. As one can notice, the coupling level measured in the frequency range from 26.5 GHz to 30 GHz is below −15 dB when the DR port is fed and below −14.2 dB when the patch port is fed. This performance has been achieved while optimizing the input reflection coefficient in such a way as to keep its

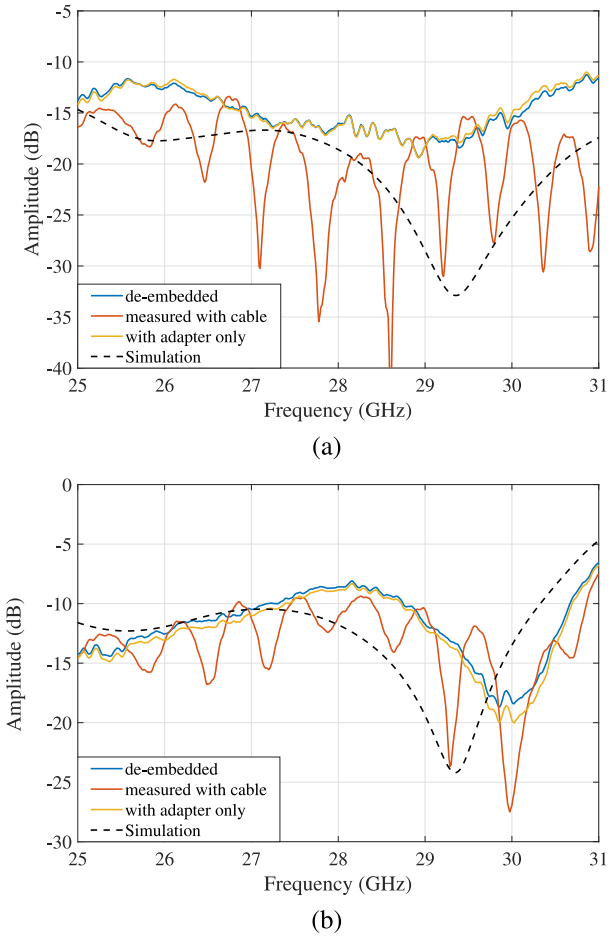

FIGURE 18. Reflection coefficient of (a) port 15 and (b) port 16 simulated vs measured.

magnitude below −11 dB (see Fig. 18b). It is worth noting here that the largest coupling level when feeding the DR port is observed towards the DR ports of the adjacent array elements. Such a parasitic process can be reduced by controlling the inter-element spacing.

For a more complete characterization of the array structure, the active reflection coefficient was simulated and compared to the measurement results. The active reflection coefficient (Γ_A) at the individual antenna port is evaluated through the following expression [24]:

$$\Gamma_A = \sum_{n=1}^{N} \frac{a_n}{b_m} S_{mn} = \sum_{n=1}^{N} \frac{|a_n| e^{j\psi_n}}{|b_m| e^{j\psi_m}} S_{mn}, \tag{10}$$

with ψ_m and ψ_n denoting the feeding phase at the $m-th$ and $n-th$ port, respectively. To evaluate the total active reflection coefficient of the individual antenna element (Γ_{A_E}) we then combine the Γ_A relevant to the two ports of each element as follows [25]:

$$|\Gamma_{A_E}| = \sqrt{\frac{|\Gamma_{A_1}|^2 + |\Gamma_{A_2}|^2}{2}}. \tag{11}$$

TABLE 2. Linear antenna arrays with wide-angle scanning capabilities available in the scientific literature for 5G wireless communications.

Ref.	Antenna technology	Frequency (GHz)	Impedance bandwidth (%)	Peak Gain (dBi)	Volume (mm^3)	Scanning capability	N° antennas
[15]	Vivaldi	26	12.5	11	$30 \times 8.8 \times 0.64$ $(6\lambda_0 \times 1.76\lambda_0 \times 0.13\lambda_0)$	-60° ∼ 60°	1 × 4
[16]	Patch	26	16	10.4	$18.2 \times 4.1 \times 1.07$ $(3.64\lambda_0 \times 0.82\lambda_0 \times 0.214\lambda_0)$	-60° ∼ 60°	1 × 4
[18]	Folded Slot	38	5.3	7.7	$15.6 \times 1.8 \times 0.89$ $(3.12\lambda_0 \times 0.36\lambda_0 \times 0.18\lambda_0)$	-50° ∼ 50°	1 × 4
[17]	Patch	26	15.4	16.5	$47.1 \times 8 \times 0.8$ $(9.4\lambda_0 \times 1.6\lambda_0 \times 0.16\lambda_0)$	-60° ∼ 60°	1 × 12
[19]	Stacked Patch	26.5	41.5	12.1	$52.8 \times 6.6 \times 3.11$ $(10.56\lambda_0 \times 1.32\lambda_0 \times 0.62\lambda_0)$	-65° ∼ 65°	1 × 8
[20]	SIW Loop Loaded	28	10	9.51	$124.5 \times 105 \times 3.048$ $(24.9\lambda_0 \times 21\lambda_0 \times 0.61\lambda_0)$	-48° ∼ 48°	1× 4
[21]	Inverted L	31	32	6.1 /8.1	$14.4 \times 10.1 \times 0.4$ $(2.9\lambda_0 \times 2.02\lambda_0 \times 0.08\lambda_0)$	-60° ∼ 60°	1 × 4
					$29 \times 10.1 \times 0.4$ $(5.8\lambda_0 \times 2.02\lambda_0 \times 0.08\lambda_0)$	-55° ∼ 55°	1 × 8
[22]	Differentially Fed Dipole	29	26.5	13.5	$44 \times 28.5 \times 1.72$ $(8.8\lambda_0 \times 5.7\lambda_0 \times 0.35\lambda_0)$	-60° ∼ 60°	1 × 8
This work	**Dual-Port Hybrid DR / Patch**	**28**	**14.8**	**15**	**$80 \times 22.6 \times 4.88$ $(16\lambda_0 \times 4.52\lambda_0 \times 0.98\lambda_0)$**	**-75° ∼ 75°**	**1 × 16**

The total active reflection coefficient of the individual array element is shown in Fig. 20 for different scan angles from 0° to 75° from 25 GHz to 30 GHz. Because of the symmetry of the array structure, only the results related to one sub-space are reported in Fig. 20a and Fig. 20b. As can be noticed, the measured results are somehow worse than the simulated ones. The suboptimal performance of the active reflection coefficients is attributed to manufacturing tolerances. These tolerances can introduce variations in the physical properties of the components, leading to deviations from the desired specifications. While we made efforts to minimize these tolerances during the manufacturing process, some discrepancies may still arise, resulting in non-ideal active reflection coefficients. However, it is worth highlighting that despite these limitations, the prototype implementation successfully allowed us to validate our design concept and evaluate the realized gain of the proposed antenna array. The measured realized gain, as demonstrated in our research study (see Fig. 14 and Fig. 15), exhibits characteristics that are closely in line with our expectations and numerically simulated predictions. This indicates that while the active reflection coefficients may not be optimal, the overall system performance, as reflected by the measured radiation pattern properties, confirms the benefits of our design strategy. In this context, one can notice that the magnitude of the active reflection coefficient remains below −7 dB (equivalent to a VSWR of approximately 2.6:1) throughout the entire scan range and operating frequency band of the array.

The measured scan performance of the array is documented in Fig. 21. Here the field of view is divided into two sub-spaces, as anticipated in the previous sections. One can notice that thanks to the low gain of the radiating mode in the opposite direction to the main beam, the secondary radiation lobes, as well as any possible undesired grating lobes, are drastically attenuated. This favorable characteristic is even more visible in the color map shown in Fig. 22, where the side-lobe level is plotted as a function of frequency and main-lobe direction. It is worth mentioning here that the proposed antenna array design is not subject to grating lobes.

IV. DISCUSSION

The design solution detailed in this research study has been benchmarked against the current state of the art for phased array antennas with wide scanning capabilities, as documented in the scientific literature. As shown in Table 2, the majority of existing solutions are limited to a scan range of up to ±60°, whereas the proposed array solution extends the scan range to ±75°.

While Table 2 indicates comparable overall performance, we would like to emphasize that our design achieves a significantly wider beam scan range.

In comparison to previous works, such as [22], our design incorporates a multi-port antenna solution that enables fine control of the radiation pattern at the individual element level through phase shifting, in such a way to support two radiating modes.

Each mode features maximum radiation at approximately +/– 40°, in contrast to the ideal case, where the maximum

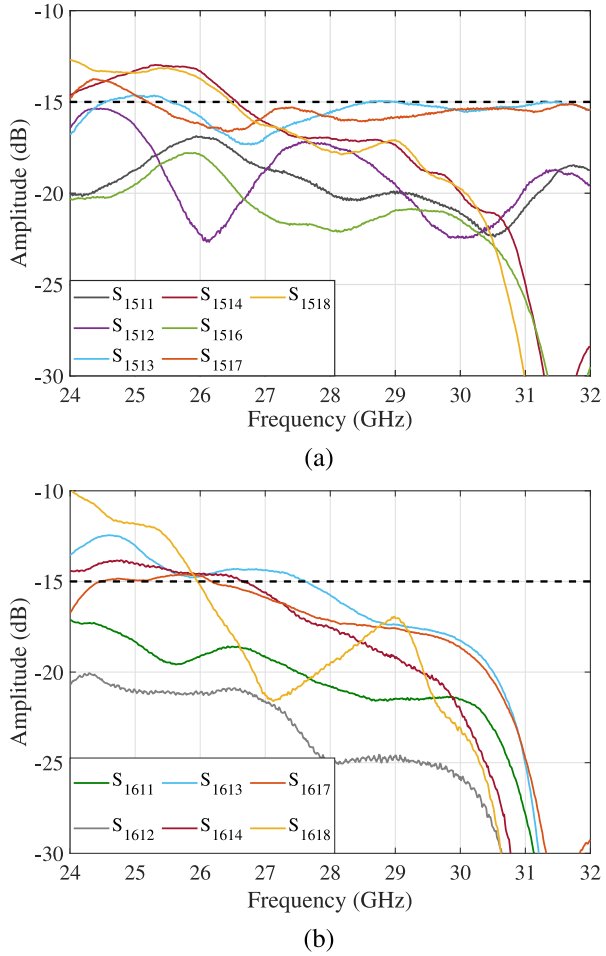

FIGURE 19. Coupling coefficients of (a) port 15 and (b) port 16 with the adjacent elements.

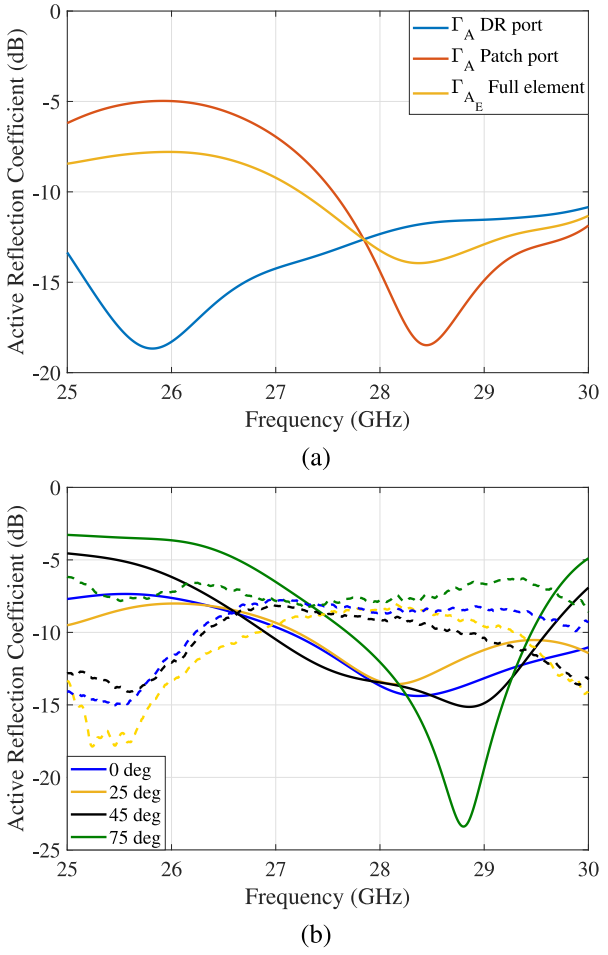

FIGURE 20. Active reflection coefficient of the central element when radiating (a) in broadside and (b) while scanning, with simulations in solid lines and measurements in dashed lines.

radiation is typically observed along the boresight. The latter limits the beam-steering capabilities at the antenna-array level, resulting in a narrower scan range. With our approach instead, by combining these modes, we are able to generate multiple lobes that can be steered independently, thus allowing for a significantly wider scan range at array level. This unique feature enables the proposed antenna array to surpass the performance of the ideal case without the need for complex or expensive technical solutions in the design.

Furthermore, as shown in [1], the degradation of the realized gain featured by a conventional phased array outside the relevant scan range is very sharp and severe, whereas our array design is characterized by a limited gain loss of 3 dB over a very wide scan range from $-75°$ to $+75°$, and of about 6 dB in the even broader angular range from $-85°$ to $+85°$.

The increased scan range is a key feature of our technical proposal that enables greater coverage and flexibility in practical applications. We believe that the enhanced performance sets our design apart from existing approaches and offers distinct advantages in terms of system capabilities.

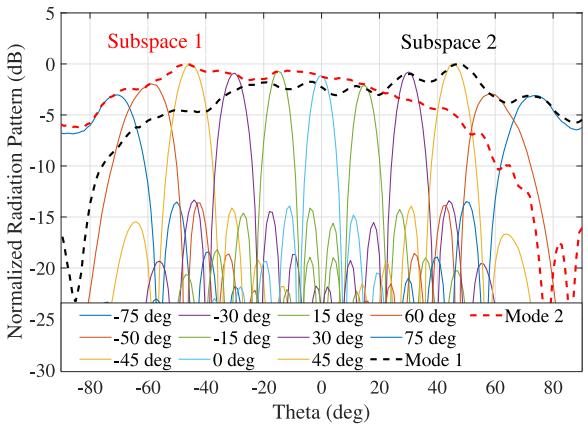

FIGURE 21. Measured scan range of the linear array at 28 GHz.

V. CONCLUSION

In this paper, a novel wide-scanning linear antenna array with multi-mode characteristics is presented. Such an array is based on a novel dual-fed antenna element that can support two radiating modes by controlling the phase difference between the two relevant input ports. The proposed antenna

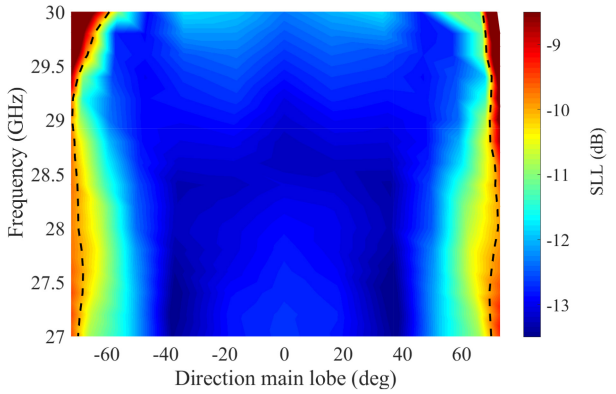

FIGURE 22. Side lobe levels of the linear array while scanning versus frequency as a function of the main-lobe direction.

is realized by integrating, in the same physical structure, a capacitively fed patch with a cylindrical dielectric resonator mounted on top of it. By introducing a phase offset of 180° between the antenna ports, the embedded element pattern can be steered in such a way as to cover two complementary sub-spaces, the first one from −75° to +20° and the second one from −20° to +75°. Thanks to these characteristics, the developed antenna array is able to scan from −75° to +75° with a gain loss smaller than 3 dB (or from −85° to +85° with a loss below 6 dB), while most of the alternative array solutions available in the scientific literature cannot scan beyond ±60°. Furthermore, the proposed design is characterized by a peak side lobe level always below −9.5 dB. Measurement results showed a wide operating frequency band from 27 GHz to 29.5 GHz with an active return loss above 7 dB across the entire scan range.

REFERENCES

[1] G. Federico, D. Caratelli, G. Theis, and A. B. Smolders, "A review of antenna array technologies for point-to-point and point-to-multipoint wireless communications at millimeter-wave frequencies," *Int. J. Antennas Propag.*, vol. 2021, Apr. 2021, Art. no. 5559765, doi: 10.1155/2021/5559765.

[2] S. E. Valavan, D. Tran, A. G. Yarovoy, and A. G. Roederer, "Planar dual-band wide-scan phased array in X-band," *IEEE Trans. Antennas Propag.*, vol. 62, no. 10, pp. 5370–5375, Oct. 2014, doi: 10.1109/TAP.2014.2343252

[3] G. Yang, J. Li, R. Xu, Y. Ma, and Y. Qi, "Improving the performance of wide-angle scanning array antenna with a high-impedance periodic structure," *IEEE Antennas Wireless Propag. Lett.*, vol. 15, pp. 1819–1822, 2016, doi: 10.1109/LAWP.2016.2537850.

[4] R. Wang, B. Z. Wang, C. Hu, X. Ding, "Wide-angle scanning planar array with quasi-hemispherical-pattern elements," *Sci. Rep.*, vol. 7, p. 2729, Jun. 2017, doi: 10.1038/s41598-017-03005-3.

[5] G. Yang, J. Li, S. G. Zhou, and Y. Qi, "A wide-angle E-plane scanning linear array antenna with wide beam elements," *IEEE Antennas Wireless Propag. Lett.*, vol. 16, pp. 2923–2926, 2017, doi: 10.1109/LAWP.2017.2752713.

[6] G. Yang, J. Li, D. Wei, and R. Xu, "Study on wide-angle scanning linear phased array antenna," *IEEE Trans. Antennas Propag.*, vol. 66, no. 1, pp. 450–455, Jan. 2018, doi: 10.1109/TAP.2017.2761999.

[7] B. Ahn et al., "Wide-angle scanning phased array antenna using high gain pattern reconfigurable antenna elements," *Sci. Rep.*, vol. 9, p. 18391, Dec. 2019, doi: 10.1038/s41598-019-54120-2.

[8] F. Sun and S. He, "Extending the scanning angle of a phased array antenna by using a null-space medium," *Sci. Rep., 4*, vol. 6832, pp. 1–6, Oct. 2014, doi: 10.1038/srep06832.

[9] F. Sun, S. Zhang, and S. He, "A general method for designing a radome to enhance the scanning angle of a phased array antenna," *Prog. Electromagn. Res.*, vol. 145, pp. 203–212, Mar. 2014, doi: 10.2528/PIER14030702.

[10] J. B. Pendry, D. Schurig, and D. R. Smith, "Controlling electromagnetic fields," *Science* vol. 312, pp. 1780–1782, Jun. 2006.

[11] "5G mmwave NXP Semiconductors." Accessed: Nov. 18, 2022. [Online]. Available: https://www.nxp.com/products/radio-frequency/5g-mmwave:5G-mmWave

[12] Y. M. Pan, K. W. Leung, and L. Guo, "Compact laterally radiating dielectric resonator antenna with small ground plane," *IEEE Trans. Antennas Propag.*, vol. 65, no. 8, pp. 4305–4310, Aug. 2017, doi: 10.1109/TAP.2017.2712807.

[13] S. Long, "A combination of linear and slot antennas for quasi-isotropic coverage," *IEEE Trans. Antennas Propag.*, vol. AT-23, no. 4, pp. 572–576, Jul. 1975, doi: 10.1109/TAP.1975.1141121.

[14] A. C. F. Reniers, A. Hubrechsen, G. Federico, L. A. Bronckers, and A. B. Smolders, "Spherical mm-Wave anechoic chamber for accurate far-field radiation pattern measurements," in *Proc. 52nd Eur. Microw. Conf. (EuMC)*, Milan, Italy, 2022, pp. 318–321, doi: 10.23919/EuMC54642.2022.9924456.

[15] R. Rodriguez-Cano, S. Zhang, K. Zhao, and G. F. Pedersen, "Reduction of main beam-blockage in an integrated 5G array with a metal-frame antenna," *IEEE Trans. Antennas Propag.*, vol. 67, no. 5, pp. 3161–3170, May 2019, doi: 10.1109/TAP.2019.2900407.

[16] Y. He, S. Lv, L. Zhao, G.-L. Huang, X. Chen, and W. Lin, "A compact dual-band and dual-polarized millimeter-wave beam scanning antenna array for 5G mobile terminals," *IEEE Access*, vol. 9, pp. 109042–109052, 2021, doi: 10.1109/ACCESS.2021.3100933.

[17] M. Stanley, Y. Huang, H. Wang, H. Zhou, A. Alieldin, and S. Joseph, "A capacitive coupled patch antenna array with high gain and wide coverage for 5G smartphone applications," *IEEE Access*, vol. 6, pp. 41942–41954, 2018, doi: 10.1109/ACCESS.2018.2860795.

[18] J. Park, H. Seong, Y. N. Whang, and W. Hong, "Energy-efficient 5G phased arrays incorporating vertically polarized endfire planar folded slot antenna for mmWave mobile terminals," *IEEE Trans. Antennas Propag.*, vol. 68, no. 1, pp. 230–241, Jan. 2020, doi: 10.1109/TAP.2019.2930100.

[19] L. Wang et al., "Wideband dual-polarized binary coding antenna with wide Beamwidth and its array for millimeter-wave applications," *IEEE Antennas Wireless Propag. Lett.*, vol. 19, no. 4, pp. 636–640, Apr. 2020, doi: 10.1109/LAWP.2020.2974160.

[20] Y. Zhu and C. Deng, "Millimeter-wave dual-polarized multibeam endfire antenna array with a small ground clearance," *IEEE Trans. Antennas Propag.*, vol. 70, no. 1, pp. 756–761, Jan. 2022, doi: 10.1109/TAP.2021.3098545.

[21] J.-Y. Lee, J. Choi, D. Choi, Y. Youn, and W. Hong, "Broadband and wide-angle scanning capability in low-coupled mm-Wave phased-arrays incorporating ILA with HIS fabricated on FR-4 PCB," *IEEE Trans. Veh. Technol.*, vol. 70, no. 3, pp. 2076–2088, Mar. 2021, doi: 10.1109/TVT.2021.3061897.

[22] I. Syrytsin, S. Zhang, G. F. Pedersen, and A. S. Morris, "Compact quad-mode planar phased array with wideband for 5G mobile terminals," *IEEE Trans. Antennas Propag.*, vol. 66, no. 9, pp. 4648–4657, Sep. 2018, doi: 10.1109/TAP.2018.2842303.

[23] V. Issakov, W. Maciej, T. Andreas, and M. Linus, "Extension of Thru de-embedding technique for asymmetrical and differential devices," *IET Circuits Devices Syst.*, vol. 3, pp. 91–98, May 2009, doi: 10.1049/iet-cds.2008.0276.

[24] A. D. Brown, "Array elements," in *Active Electronically Scanned Arrays: Fundamentals and Applications*. Hoboken, NJ, USA: IEEE Press, 2022, pp. 75–101, doi: 10.1002/9781119749097.

[25] E. Fritz-Andrade, H. Jardon-Aguilar, and J. A. Tirado-Mendez, "The correct application of total active reflection coefficient to evaluate MIMO antenna systems and its generalization to N ports," *Int. J. RF Microw. Comput.-Aided Eng.*, vol. 30, no. 4, Art. no. e22113, 2020, doi: 10.1002/mmce.22113.

GABRIELE FEDERICO (Member, IEEE) received the B.Sc. and M.Sc. degrees in telecommunication engineering from the University of Bologna, Italy, in 2013 and 2016, respectively, and the P.D.Eng. degree from the Eindhoven University of Technology in 2018, where he is currently pursuing the Ph.D. degree with Electromagnetics Group. His research interests include antenna measurements, antenna array design for mm-wave wireless communications, and RF material characterization.

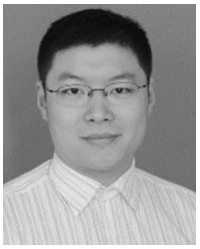

ZHE SONG (Senior Member, IEEE) received the B.S. and Ph.D. degrees in radio engineering and microwave engineering from Southeast University, Nanjing, China, in 2005 and 2011, respectively, where he was a Lecturer and a Researcher with the State Key Laboratory of Millimeter Waves and the School of Information Science and Engineering from 2011 to 2016. From 2017 to 2019, he was a Postdoctoral Research Fellow with the Mixed-Signal Microelectronics Group and the Electromagnetics Group, Department of Electrical Engineering, Eindhoven University of Technology (TU/e), Eindhoven, The Netherlands, respectively. From 2019 to 2021, he was a Guest Researcher with the EM Group, Department of Electrical Engineering, TU/e and a Senior RF/Antenna Engineer with The Antenna Company, Eindhoven. Since 2021, he has been a Staff RFFE Module Engineer with Qualcomm, Nijmegen, The Netherlands. He has research experiences in generalized multilayer Green's function, Maxwell integral equation, method of moments, and high-performance computing on GPU/CPU heterogeneous platforms. He has design and test experiences in low noise amplifier, distributed amplifier, variable gain amplifier, RF-switch, RF filter, and ultrawideband power divider based on GaAs, SiGe BiCMOS, and RF-SOI technologies, as well as sub-6 GHz RF front-end module, mm-wave phased array, UWB and MIMO system implementation based on advanced laminate, and PCB technologies. His current research interests include RFIC, MMIC, RF front-end module, nonlinear circuit modeling, and multiobjective optimization for RF circuits and systems.

GUILHERME THEIS (Graduate Student Member, IEEE) received the B.Sc. degree in electrical engineering from the University of Paraná Curitiba, Brazil, the M.Sc. degree in electronic systems from the University of Bordeaux, and the engineering degree in radio and telecommunication systems from ENSEIRB-MATMECA, Bordeaux, France, in 2019. He is currently pursuing the Ph.D. degree with the Eindhoven University of Technology, Eindhoven, The Netherlands. His research interest includes development of 5G systems, with focus on millimeter-wave antenna array and subarray design.

DIEGO CARATELLI (Senior Member, IEEE) was born in Latina, Italy, in 1975. He received the M.Sc. degree (summa cum laude) in applied mathematics and the Laurea (summa cum laude) and Ph.D. degrees in electronic engineering from the Sapienza University of Rome, Rome, Italy, in 2000, 2004, and 2013, respectively. From 2005 to 2007, he was a Research Fellow with the Department of Electronic Engineering, Sapienza University of Rome. From 2007 to 2013, he was a Senior Researcher with the International Research Center for Telecommunications and Radar, Delft University of Technology, Delft, The Netherlands. From 2015 to 2019, he was an Associate Professor with the Institute of Cybernetics, Tomsk Polytechnic University, Tomsk, Russia. In 2013, he co-founded The Antenna Company, Eindhoven, The Netherlands, where he is currently the Chief Technology Officer/Vice-President of Engineering and is responsible for product development, program portfolio management, and technical direction of the engineering team. Since 2020, he has been an Associate Professor with the Group of Electromagnetics in Wireless Telecommunications, Eindhoven University of Technology, Eindhoven. He has authored or coauthored more than 200 publications in international peer-reviewed journals, book chapters, and conference proceedings. He holds 22 families of patents in antenna-related technologies and advanced computational techniques. His current research interests include the full-wave analysis and design of passive devices and antennas for satellite, wireless, and radar applications, the development of analytically based numerical techniques devoted to the modeling of wave propagation and diffraction processes, the theory of special functions for electromagnetics, the deterministic synthesis of sparse antenna arrays, and the solution of boundary-value problems for partial differential equations of mathematical physics. He was a recipient of the Young Antenna Engineer Prize at the 32nd European Space Agency Antenna Workshop and the 2010 Best Paper Award from ACES. He was a co-recipient of the Frost and Sullivan Best Practices Award for Technology Innovation in Advanced Antennas for Wireless Communications in 2016. His students received the IEEE MTT-S Central-Southern Italy Award in 2014 with Honorable Mention, the TICRA Foundation Grant, and the Honorable Mention at the IEEE AP-S/URSI Symposium in 2022. He is a Lead Guest Editor of the Special Issue on Advanced Antenna Array Development for mm-Wave Communications of *International Journal of Antennas and Propagation* (Hindawi), as well as of the Special Issue on Theory and Applications of Special Functions in Mathematical Physics of *Symmetry* (MDPI). He is currently a member of the Applied Computational Electromagnetics Society, the Institution of Engineering and Technology, the International Union of Radio Science, and the Italian Electromagnetic Society.

A. BART SMOLDERS (Senior Member, IEEE) received the Ph.D. degree in electrical engineering from the Eindhoven University of Technology (TU/e) in 1994. He is an expert in smart antenna systems and worked at TNO, THALES ASTRON, and NXP Semiconductors. Since 2010, he has been a Full Time Professor with the Electromagnetics Group, TU/e, with special interest in smart antenna systems and applications. He currently leads several large research projects in the area of integrated antenna systems for 5G/6G wireless communications. Next to his research activities, he is the Dean of the Electrical Engineering Department.